Gold Bulletin (2023) 56:145–155
https://doi.org/10.1007/s13404-023-00329-z

RESEARCH

Electrochemical sensing based on Au particle@SiO_2@CQDs nanocomposites

Huiqin Li[1] · Lihua Wu[2] · Hui Lei[1] · Cui Deng[1] · Fan Huang[1] · Lijun Ren[1] · Hongge Zhang[1] · Weiwei Zhao[1] · Qian Zhao[3]

Received: 7 December 2022 / Accepted: 15 June 2023 / Published online: 29 June 2023

Abstract

In this study, carbon quantum dots (CQDs) were first synthesized using a hydrothermal method, and then, Au@SiO_2 core-shell nanomaterials were synthesized using layer-by-layer assembly. CQDs were adsorbed on the surface of Au@SiO_2 nanoparticles through self-assembly to form Au@SiO_2/CQDs nanocomposite materials. Transmission electron microscopy and X-ray diffraction were used to characterize the size, shape, element composition, and structure of nanocomposites; ultraviolet-visible absorption spectroscopy and fluorescence spectroscopy were used to analyze the optical properties of nanocomposites. The results show that Au@SiO_2/CQD nanomaterials have a core-shell structure with good morphology and exhibit excellent luminescence characteristics. The electrochemical performance of nanocomposites was characterized using electrochemical means, and a hydrogen peroxide sensor was constructed for the sensitive detection of hydrogen peroxide, thus realizing the rapid and sensitive detection of hydrogen peroxide at levels as low as 0.2 mM. The electrode GCE modified with Au@SiO_2/CQDs exhibits good selectivity and stability in the detection of hydrogen peroxide.

Keywords Au@SiO_2/CQDs nanocomposites · Carbon quantum dots · Hydrogen peroxide · Electrochemical sensing

Introduction

H_2O_2 is a signal molecule that can regulate various biological processes such as immune cell activation [1] and cell imaging [2]. However, excess H_2O_2 can interfere with the conduction of other signaling, which can cause diseases such as cardiovascular disease, Alzheimer's disease, and cancer. Therefore, it is very important for H_2O_2 detection. Various measurement methods for H_2O_2 have been explored, including fluorescence detection [3] and chemiluminescence [4]. Among them, the electrochemical method [5] has the advantages of simple operation, high detection sensitivity, and fast response speed. Therefore, a type of H_2O_2 sensor was constructed to be used for the sensitive detection of H_2O_2 [6].

Carbon quantum dots (CQDs) are a type of 0D nanomaterials with a size of < 10 nm [7]. It has the advantages of high fluorescence intensity, good photostability, wide excitation spectrum and narrow emission spectrum, large Stokes shift, long fluorescence lifetime, and good biocompatibility [8]. Therefore, it has great application prospects in fluorescence detection [9], biological imaging [10], biosensor [11], and medicine [12]. Among the multiple properties of CQDs, the most attractive one is its unique optical properties. It can be used as an electrochemiluminescent material; however, because of its own surface defects, its electrochemiluminescence intensity is low.

With the development of nanomaterials, precious metal nanomaterials have attracted considerable attention. Au nanomaterials have a local surface plasmon resonance (LSPR) effect. At the resonance wavelength, Au nanoparticles both scatter and absorb incident light. LSPR excitation will produce an enhanced electromagnetic field around nanoparticles [13, 14] and will have an impact on the properties of the nanomaterials around Au nanoparticles. Coating

✉ Huiqin Li
huiqinli@yeah.net

✉ Lihua Wu
wulihua198383@163.com

[1] Department of Chemistry and Chemical Engineering, Baoji University of Arts and Sciences, Baoji 721013, Shaanxi, China

[2] Hebei Construction Material Vocational and Technical College, Qinhuangdao 066004, Hebei, China

[3] Shaanxi Key Laboratory of Disaster Monitoring and Mechanism Simulation, Baoji University of Arts and Sciences, Baoji 721013, Shaanxi, China

CQDs on the surface of Au@SiO_2, based on the SPR of Au nanoparticles, the luminous efficiency of CQDs is considerably improved. SiO_2 acts as a spacer between Au core and CQDs [15]; by adjusting the thickness of SiO_2 shell, Au nanoparticles can either enhance or quench the properties of CQDs because of the optical transparency and biocompatibility of SiO_2. Moreover, the SiO_2 coating will not affect the properties of Au nanoparticles and CQDs, and SiO_2 can increase the specific surface area, improve stability and provide modification sites for the easier modification of functional groups such as amino and carboxyl groups [16, 17]. For hydrogen peroxide sensors, the synergy between CQDs and Au@SiO_2 enables Au@SiO_2/CQD nanocomposites to exhibit excellent electrochemiluminescence performance and can be used as an ideal material.

This study reports a method for preparing Au@SiO_2/CQD nanocomposite, along with the electrochemiluminescence of CQDs and the detection signal amplification of Au@SiO_2. Furthermore, it can be used for developing hydrogen peroxide sensors and sensitive detection of different concentrations of hydrogen peroxide.

Experimental

Chemicals

Chloroauric acid ($HAuCl_4{\cdot}4H_2O$, 99.999%), cetyltrimethylammonium bromide (CTAB, 99.0%), sodium hydroxide (NaOH, >96%), formaldehyde (CH_4O, 37.0%), tetraethyl orthosilicate (TEOS, >98.0%), methanol (CH_3O, 99.7%), ethanol (C_2H_6O, 95.0%), glucose monohydrate ($C_6H_{12}O_6{\cdot}H_2O$), chloroacetic acid ($C_2H_3ClO_2$, 99.5%), 3-aminopropyl) trimethoxysilane (APTES, 97%), hydrogen peroxide (H_2O_2, 30%), and deionized water were used for all experiments.

Synthesis of carbon quantum dots

The CQD solution was synthesized using a hydrothermal method. For this purpose, weigh 1 g of glucose, add 25 mL of deionized water, stir at room temperature for 10 min, and, after all particles are dissolved, transfer to a polytetrafluoroethylene reactor for reaction in a drying oven.

Subsequently, weigh 1 g of glucose, add 12.5 mL of ethanol, and 12.5 mL of deionized water, stir at room temperature for 10 min, and, after all particles are dissolved, transfer to a polytetrafluoroethylene reactor for reaction in a drying oven.

Both reaction solutions changed the reaction time (2, 4, 6, and 8 h) and changed the reaction temperature (160 °C, 180 °C, and 200 °C). After the reaction, pure carbon was obtained using centrifugation and suction, and the QD solution was stored at 4 °C for later use.

Synthesis of Au@SiO_2 nanoparticles

CTAB (0.05 g) was dissolved in deionized water (24 mL), and then 0.5 mol/L of NaOH solution was added. The reaction was conducted in a water bath at 80 °C for 15 min, and then 412 µL of 0.048 mol/L $AuCl_4{\cdot}4H_2O$ solution and 500 µL of formaldehyde solution were added. In a few seconds, the solution changed from colorless to wine red and then reacted for 10 min to obtain Au nanoparticles.

Subsequently, the mixture of ethyl orthosilicate and methanol (mol% = 4:1) was allowed to react for 6 h, centrifuged, and then washed with ethanol and deionized water at 8000 rpm for three times to obtain Au@SiO_2 nanoparticles [18].

Synthesis of Au@SiO_2/CQD nanocomposite

The synthesis of Au@SiO_2/CQD nanoparticles is divided into three steps:

(1) Hydroxylation of CQDS: Accurately weigh NaOH (0.005 g) and chloroacetic acid (0.01 g) into pure CQDS solution (2 mL), followed by ultrasonication for 3 h. Then, ensure the water temperature remains constant during ultrasonication.
(2) Amination of Au@SiO_2 nanoparticles [19]: Disperse 2 mL of Au@SiO_2 nanomaterials in 20 ml of ethanol, add 2 µL APTES, stir at room temperature for 24 h, and centrifuge for washing.
(3) Adsorption of CQDs on Au@SiO_2 surface: Disperse hydroxyl-functionalized CQDs and amino-functionalized Au@SiO_2 in ethanol (20 mL), stir at room temperature for 12 h, and centrifuge and wash to remove unadsorbed CQDs solution to obtain Au@SiO_2/CQD nanoparticles.

Electrode preparation and electrochemical measurement

Using a three-electrode system, electrochemical characterization and analysis were performed on the CHI660c electrochemical analyzer. The working electrode was a glassy carbon electrode covered with Au@SiO_2/CQD nanomaterials, the reference electrode was an Ag/AgCl electrode, and the counter electrode was a Pt electrode. Electrolyte solution: 0.1 mol/L KCl solution and 2 mmol/L $K_3[Fe(CN)_6]$ solution prepared now.

Electrode preparation: A glassy carbon electrode (GCE, $\Phi = 3$ mm) was subsequently polished with 0.3-µm alumina slurry. The GCE was ultrasonically cleaned with ethanol and deionized water and dried at room temperature. Moreover, the solutions of CQDs (5 µL) and Au@SiO_2/CQDs (5 µL)

were subsequently dropped on the GCE, and then dried at room temperature. H_2O_2 detection was performed using a time–current curve.

Characterization

Transmission electron microscopy (TEM) and high-resolution transmission analysis were performed at an accelerating voltage of 200 kV using Tecnai G2 F20 S-TWIN field-emission transmission electron microscope (FEI Company, USA). UV-2550 UV-Vis spectrophotometer (Shimadzu) was used for UV-vis absorption analysis. Fluoromax-4 steady-state/transient fluorescence spectrometer (HJY Company, France) was used to test the fluorescence spectrum. X-ray diffraction (XRD) analysis was performed using the DMAX U1TIMAIV X-ray diffractometer (Rigaku). Cyclic voltammetry curves and AC impedance spectra were obtained using CHI660c electrochemical workstation (Shanghai Chenhua Instrument Co., Ltd.). The time–current curve was obtained using German Zahner electrochemical workstation.

Results and discussion

Characterization of CQDs

Figure 1 shows the CQDs synthesized using a hydrothermal method and characterized by TEM. The figure shows that the synthesized CQDs are quasi-spherical with good dispersion and no aggregation. From Fig. 1b (inset), the lattice fringes of CQDs can be clearly observed, which corresponds to the (002) reflection of graphitic carbon [20]. The size of CQDs is approximately between 2 and 3.5 nm, and the average particle size is 2.85 nm through particle size statistical analysis.

Figure 2 shows the optical properties of CQDs are characterized by fluorescence and ultraviolet spectroscopy. Figure 3a shows the UV absorption spectrum of CQDs. There is obvious absorption in the ultraviolet region, and the maximum absorption peak is at 283 nm. This is attributed to the n-π* transition of the C=O bond, and the π-π* transition of the conjugated C=C. Figure 2b shows the fluorescence spectrum of CQDs. With excitation from 320 to 420 nm, the emission peak position red-shifted from 406 to 478 nm, indicating that the prepared CQDs have excitation wavelength dependence, which may be attributed to the difference of light selectivity of differently sized nanoparticles [21]. Moreover, the excitation light has a wide wavelength range and a large Stokes shift [22], which can effectively avoid the overlap of emission and excitation spectrums [23]. These characteristics are consistent with the literature reports and can meet the requirements of further application.

When using glucose as carbon source and deionized water as solvent to synthesize CQD-based solution, the fluorescence spectrum obtained is shown in Fig. 2c. The fluorescence intensity of CQD-based solution increased with increase in reaction time, and the highest fluorescence intensity was obtained at 8 h. Because the reaction temperature increased, the fluorescence intensity increased in sequence, and the fluorescence intensity was the strongest at 200 °C. When using glucose as carbon source and ethanol and deionized water as solvents to synthesize CQD-based solution, the fluorescence spectrum obtained is shown in Fig. 2c. The fluorescence intensity of CQDs first increased and then decreased with extension of reaction time. The highest fluorescence intensity was obtained at 4 h. As the reaction temperature increased, the fluorescence intensity sequentially increased and the fluorescence intensity was strongest at 200 °C. From the comparison between these two figures, when ethanol is added to the solvent, the fluorescence intensity is significantly higher than that of CQDs synthesized using only deionized water as the solvent. Because of the high fluorescence intensity and low requirements of experimental conditions, CQDs synthesized with ethanol and water as solvents for subsequent experiments.

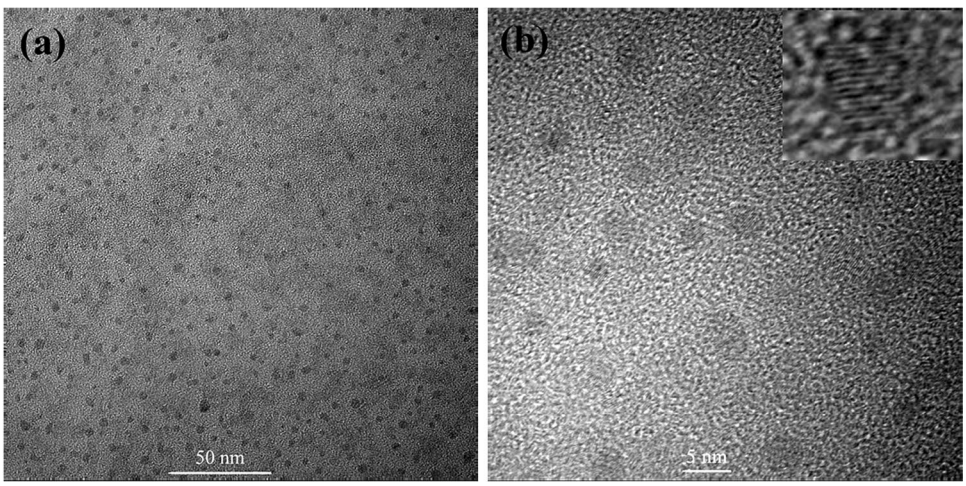

Fig. 1 **a** TEM images of CQDs with different magnification factor and (**b**) high-resolution images of carbon quantum dots inserted

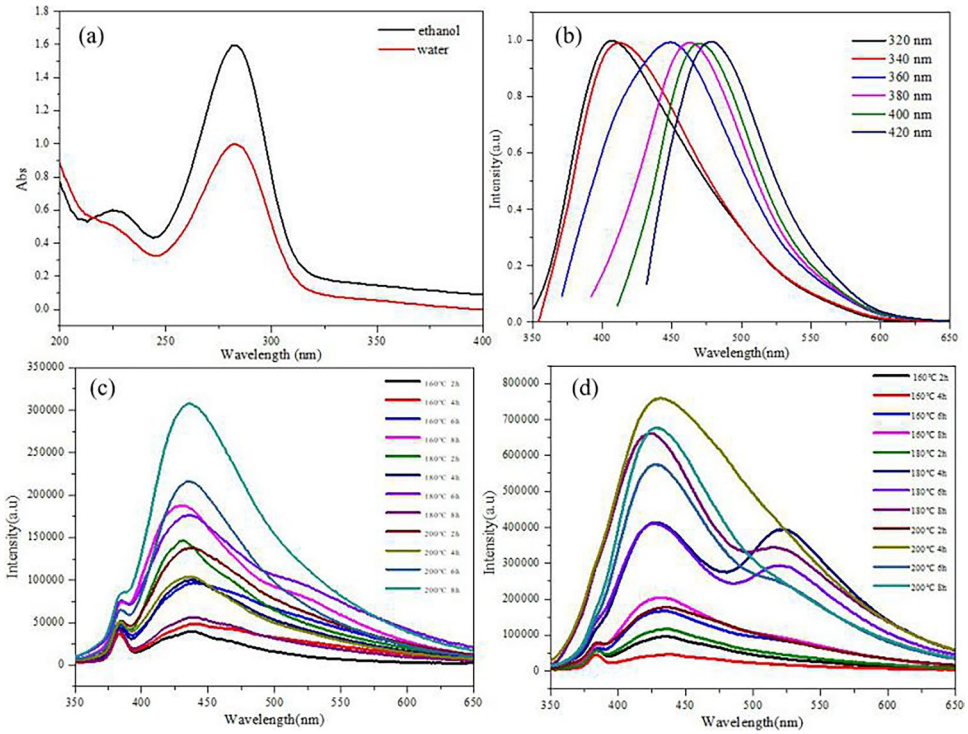

Fig. 2 **a** UV-vis spectra of CQDs synthesized with ethanol and water as solvents; **b** fluorescence spectra of CQDs at different excitation wavelengths; the fluorescence spectra of CQDs synthesized with water as a solvent (**c**) and ethanol as a solvent (**d**) at different reaction temperatures and times were studied

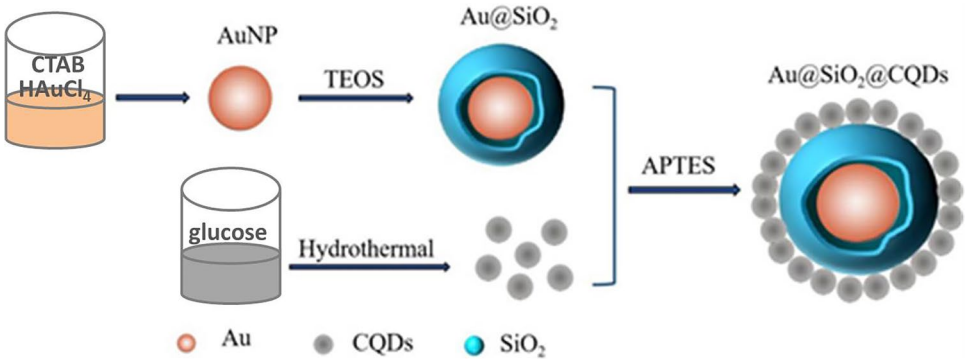

Fig. 3 Schematic diagram of the synthesis process of Au@SiO_2/CQDs nanocomposites

Synthesis of Au@SiO_2 nanoparticles and coating of CQDs

Figure 3 shows the fabrication of Au@SiO_2/CQDs nanocomposites. At first, Au nanoparticles were synthesized by the reduction of chloroauric acid with CTAB as a template. Then, by adding tetraethyl orthosilicate, the surface of Au nanoparticles was coated with a layer of SiO_2 shell to obtain Au@SiO_2 nanoparticles. Note that the thickness of SiO_2 shell can be adjusted by changing the amount of tetraethyl orthosilicate solution, and then (3-aminopropyl)trimethoxysilane (APTES) was added to modify the surface of SiO_2 with amino functional groups. To synthesize the CQD-based solution using a hydrothermal method, the reaction solvent, reaction temperature, and reaction time were changed, the best reaction conditions were determined, and chloroacetic acid was added to enrich the surface of CQDs with hydroxyl functional groups. To synthesize Au@SiO2/CQDs nanocomposites, amino-functionalized Au@SiO_2 nanoparticles and hydroxyl-functionalized CQDs are combined with N-H bonds.

Au@SiO_2 core-shell nanomaterials with different SiO_2 thicknesses were synthesized by changing the TEOS amount and adding ethanol. The morphology of Au@SiO_2 structure was characterized by a transmission scanning electron microscope. The TEM image obtained is shown in Fig. 4. The synthesized Au@SiO_2 nanoparticles have a nearly spherical core-shell structure. The black area in the center is the Au core; the light-colored area around the Au is the wrapped SiO_2 shell. Figure 4c (inset) is a high-resolution image of the Au core, and the lattice spacing can be clearly observed, which is 0.24 nm, and corresponds to the (111)

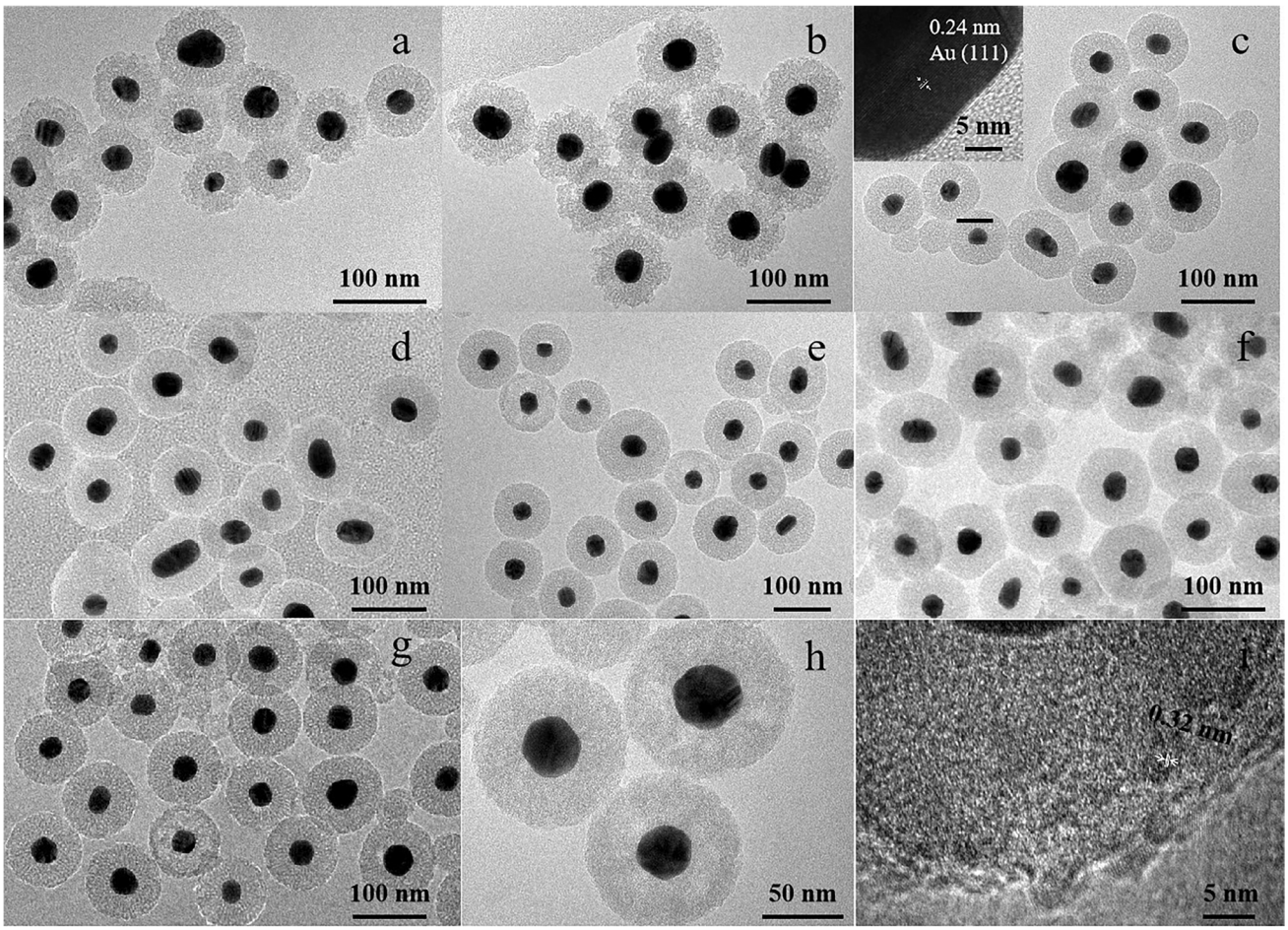

Fig. 4 TEM image of $Au@SiO_2$ core-shell nanoparticles. Add TEOS ethanol solution (**a**) 400 μL, (**b**) 500 μL, (**c**) 580 μL, (**d**) 720 μL, (**e**) 900 μL, (**f**) 1150 μL; the illustration in (**c**) is a high-resolution image of the Au core; **g–i** TEM image of $Au@SiO_2$/CQD nanocomposite structure

crystal plane of Au. When the Si source is 400 and 500 μL, Fig. 3a and Fig. 4b show that the surface of SiO_2 is rough, but the particle size distribution is uniform. With increase in the amount of Si source, the surface of SiO_2 gradually became smooth. When the amount of Si source is 1150 μL, a large number of SiO_2 spheres are formed, which indicates that the amount of Si source has reached saturation. The thickness of SiO_2 shell of $Au@SiO_2$ nanoparticles was measured using Nano Measure. Figure 5 shows the resulting particle size distribution diagram. When the amount of Si source added is 400–900 μL, the corresponding SiO_2 shell thickness average size is 24.5, 28.5, 29.9, 30.6, and 32.3 nm, respectively; the change is not obvious. Until the addition of Si source is 1150, a large number of silicon spheres appear. This indicates that the thickness of self-assembled SiO_2 has reached saturation; moreover, the growth of SiO_2 shell can be seen from the change in thickness and size. With increase in the amount of Si source added, the thickness of SiO_2 shell gradually increased. When the added amount was small, the size obviously increased. When the added amount increased from 900 to 1150 μL, the size increased became smaller. Figure 4g, Fig. 4h, and Fig. 4i shows that CQDs adsorbed on the surface of $Au@SiO_2$ core-shell structure; the lattice fringes of CQDs on SiO_2 surface can be clearly seen from the high-resolution image of Fig. 4i the lattice spacing is 0.32 nm, corresponding to the (002) crystal face of graphite carbon.

Figure 6 is the infrared spectrum of $Au@SiO_2$/CQDs, with obvious infrared peaks appearing at 3379.71 cm^{-1}, 2924.22 cm^{-1}, 2853.83 cm^{-1}, 1636.80 cm^{-1}, 1045.65 cm^{-1}, 965.11 cm^{-1}, and 784.51 cm^{-1}. Among them, the peak of 3379.71 cm^{-1} is attributed to the stretching vibration of N-H, indicating that $Au@SiO_2$ successfully aminated. The peak at 924.22 cm^{-1} is regarded as the stretching vibration of C-H in the carbon-to-carbon double bond. The peak at 2853.83 cm^{-1} belonged to the stretching vibration of C-H in – CHO, the peak of 1636.80 cm^{-1} is due to C=C stretching vibration, and the peaks at 1045.65 cm^{-1} and 965.11 cm^{-1} are attributed to Si-O stretching vibration and bending vibration, respectively. The peak at 784.51 cm^{-1} is regarded to the

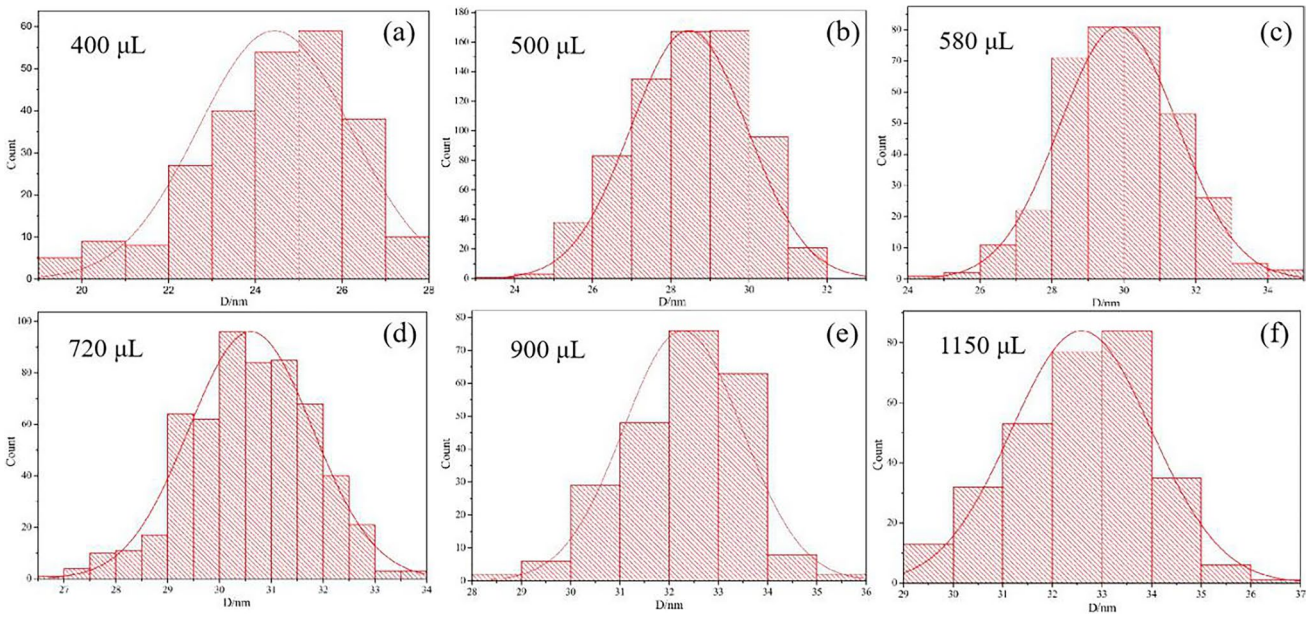

Fig. 5 The particle size distribution diagram of Au@SiO_2 nanoparticles. Add TEOS ethanol solution (**a**) 400 μL, **b** 500 μL, **c** 580 μL, **d** 720 μL, **e** 900 μL, **f** 1150 μL

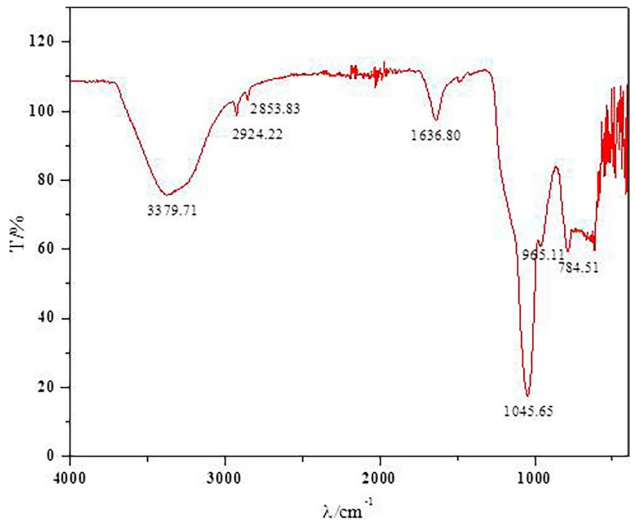

Fig. 6 The infrared spectrogram of Au@SiO2/CQDs nanoparticle

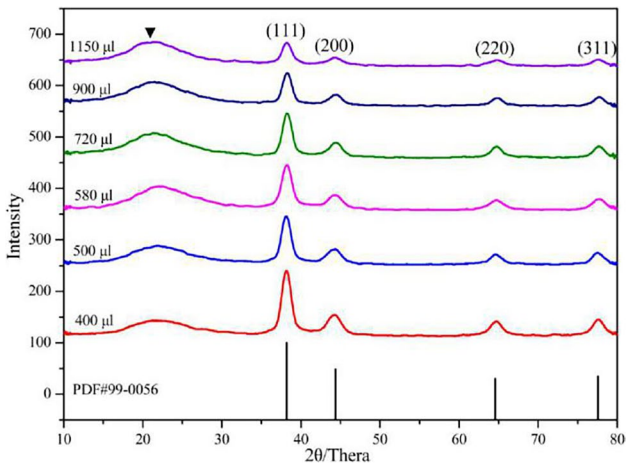

Fig. 7 XRD patterns of Au@SiO_2 nanomaterials synthesized with different TEOS ethanol solution addition amounts

out of plane bending vibration of C-H in the carbon-carbon double bond. By analyzing the infrared spectrum, it was found that the functional groups of the complex were both aminated Au@SiO_2. The N-H in, as well as the carbon-to-carbon double bond in carbon quantum dots, indicating the structure of Au@SiO_2 @ CQD composite.

Figure 7 shows the structure of Au@SiO_2 nanomaterials was analyzed by XRD. There are four distinct diffraction peaks at 38.2°, 44.4°, 64.7°, and 77.6°, corresponding to the (111), (200), (220), and (311) planes of the Au cubic face-centered phase (JCPDS card PDF#99-0056) [24]. The broad peaks marked with black triangle between 20° and 25° correspond to the SiO_2 shell (JCPDS card PDF#38-0651); the SiO_2 coated is amorphous [25]. From bottom to top in the spectrum, the Au@SiO_2 nanostructures synthesized by adding TEOS and ethanol solutions of 400, 500, 580, 720, 900, and 1150 μL as the amount of silicon source increase; namely, as the thickness of the SiO_2 shell increases, the intensity of the Au diffraction peak decreases.

The optical properties of Au@SiO_2/CQD nanocomposites were characterized using UV-vis spectroscopy. Figure 8a shows the absorption spectrum of the pure composite of

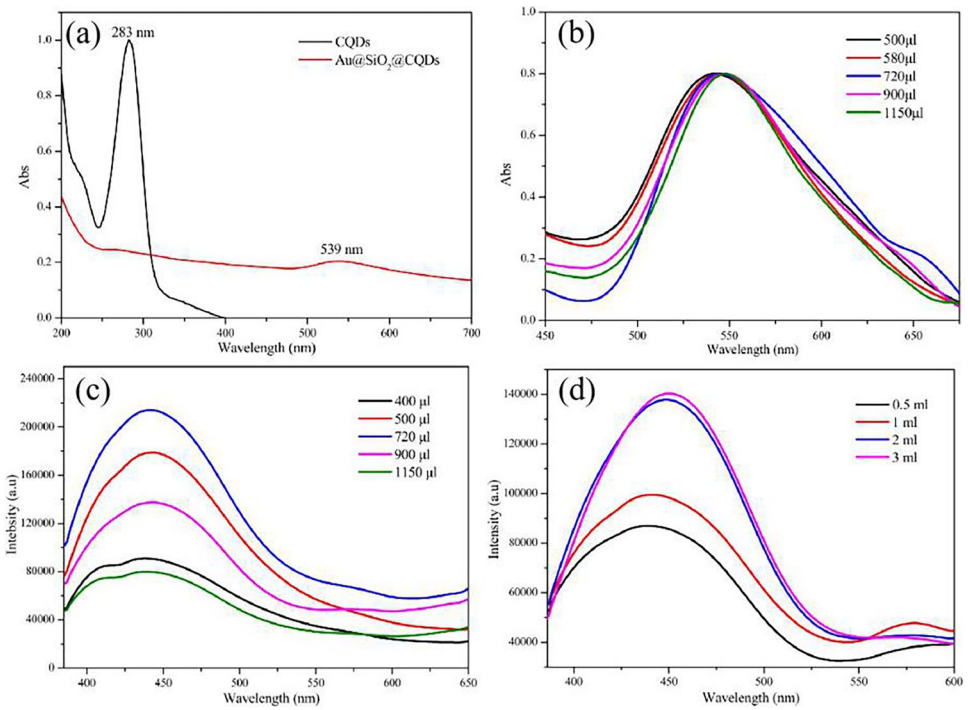

Fig. 8 **a** UV-vis spectra of CQDs and Au@SiO_2/CQD composite materials; **b** UV-vis spectrum; **c** fluorescence spectrum of Au@SiO_2/CQD composite materials with different amounts of silicon source added; **d** fluorescence spectra of Au@SiO_2/CQD composites with different CQD additions

CQDs and Au@SiO_2/CQDs. CQDs exhibit a strong absorption at 283 nm. When CQDs are adsorbed on the surface of Au@SiO_2 nanoparticles. This absorption peak disappears because of the coordination combination of hydroxylated CQDs and aminated Au@SiO_2, resulting in a change in the polarity of the coordination environment of CQDs. The Au@SiO_2/CQD composite material has an absorption peak at 539 nm, which is the SPR absorption peak of Au nanoparticles. The absorption spectrum shown in Fig 7b is obtained by adding different amounts of TEOS in ethanol to obtain nanoparticles with different SiO_2 shell thicknesses. With increase in the amount of Si source added, the absorption peak position has a slight red shift from 527 to 536 nm. This is attributed to the SPR characteristics of Au nanoparticles, which largely depends on the dielectric constant of the surrounding medium of Au nanoparticles. Because the refractive index of SiO_2 ($n = 1.4585$) is higher than that of water ($n = 1.3325$), the position of absorption peak is red-shifted after coating with SiO_2 on the surface of Au, and the thicker the SiO_2 shell, the more the redshift.

The Au@SiO_2/CQDs composite material was characterized using fluorescence spectroscopy, and the excitation wavelength was selected as 352 nm to test the emission spectrum. Figure 8c shows that the fluorescence intensity first increases, and then decreases with increase in the amount of Si source; moreover, the fluorescence intensity is the strongest at 720 μL. Compared with the hydrolysis in ethanol, the increase of SiO_2 layer thickness is not obvious, but the maximum SiO_2 thickness is about 30 nm according to the fluorescence test (Fig. 8c). Figure 8d is to prepare Au@SiO_2/CQD composite material by changing the amount of CQDs added, adding 0.5 mL, 1 mL, 2 mL, and 3 mL of CQDs, respectively, as the amount of CQDs increases, the fluorescence intensity increases. When the amount of CQDs increased from 2 to 3 mL, the increase in fluorescence intensity was not obvious; therefore, the optimal amount of CQDs was 2 mL.

Electrochemical characteristics

Electrochemical impedance technology can effectively monitor the assembly effect of electrodes. EIS comprises two parts: one part is a semicircular part representing high frequency, which can indicate the migration ability of electrons on the electrode surface. The larger the diameter of the arc, the greater the resistance of electron migration, i.e., the greater the resistance of the electrode. The other part is the low-frequency linear part, which corresponds to the diffusion process at the interface between the electrode and electrolyte [26]. After many attempts, it was found that the pH value has a significant effect on the potential of the oxidation and reduction peaks which is believed to occur due to the participation of protons in the electrode reaction [27]. When pH = 6.5, the peak performance is relatively stable, so the system studied in this article is set to pH = 6.5.

As shown in Fig. 9a, curve *m* represents the bare glassy carbon electrode, curve *n* represents CQDS-modified glassy carbon electrode, and curve *p* represents Au@SiO_2@CQD. The modified glassy carbon electrode was used as the working electrode. It can be seen from the

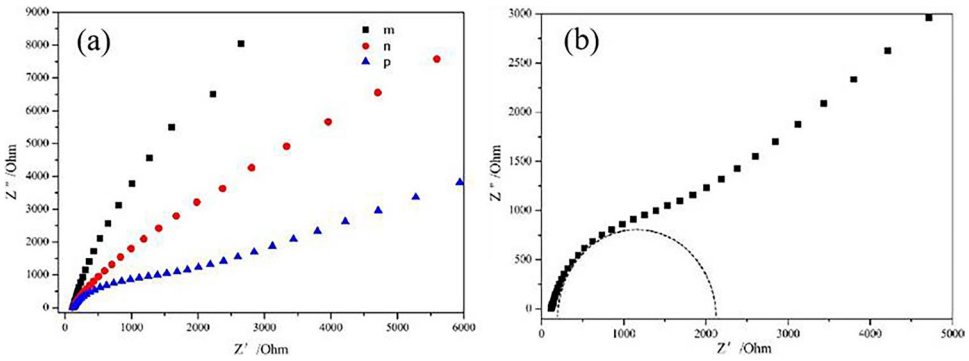

Fig. 9 **a** Electrochemical impedance spectroscopy (EIS) of m: GCE, n: CQDs/GCE, and p: Au@SiO_2/CQDs/GCE in 2.0 mmol/L $K_3[Fe(CN)_6]$ solution containing 0.1 mol/L KCl; **b** local enlarged impedance diagram of Au@SiO_2/CQDs/GCE electrode. Applied ac frequency range: 0.01 Hz to 100 kHz

figure that the electrochemical reaction resistance of bare glassy carbon electrode is the largest, and the resistance of CQDS-modified glassy carbon electrode is reduced Au@SiO_2@CQD The minimum resistance is obtained by modifying the glassy carbon electrode Au@SiO_2@CQD/GCE. The electrode resistance is roughly estimated to be 2200 Ω, indicating that Au@SiO_2@CQD. Compared with the pure CQDS, the nanocomposites have stronger electron transport capacity, and their core-shell structure is conducive to providing larger response surface and electron transfer channels [28]. Furthermore, the migration resistance of electrons on the surface of electrode changes with the change in modifier, which indicates that the modifier is successfully modified to the electrode surface and electrode is successfully assembled.

Cyclic voltammetry (CV) curves of the ferricyanide system are an effective tool to characterize the electrochemical behavior of electroactive materials on the electrode surface [29]. The electrical activities of glassy carbon electrodes modified with different materials were recorded in an electrolyte containing 2.0 mmol/L K_3 [Fe (CN) $_6$] and 0.1 mol/L KCl containing 10 mM H_2O_2, as shown in Fig. 10a. Curve *A* is bare glassy carbon electrode, showing redox peaks at 0.78 V and 0.53 V; curve *B* is CQDS-modified glassy carbon electrode, and the peak values at 0.82 V and 0.46 V are not obvious; curve *C* is Au@SiO_2/CQDs. The modified glassy carbon electrode was prepared at 0.71 V and 0.63 v. A more obvious redox peak of [Fe (CN) $_6$] $^{3-}$ was observed at v Au@SiO_2/CQDs. The modified glassy carbon electrode has fast electron transfer efficiency. The surface area

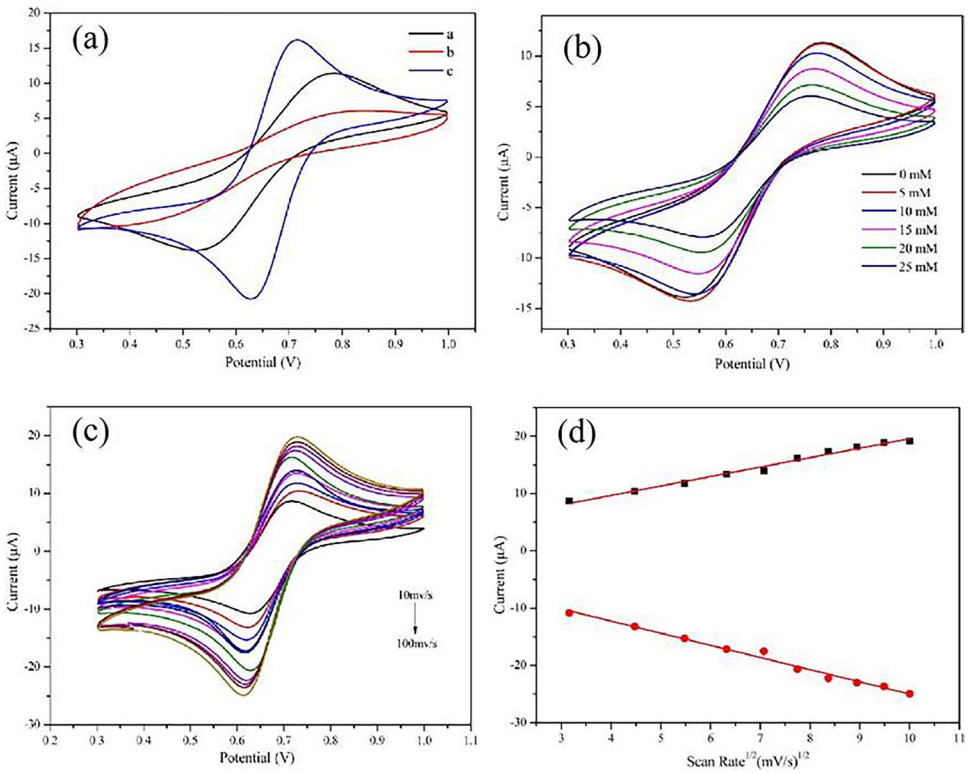

Fig. 10 **a** Bare GCE; bcqds/GCE; C with different working electrodes Au@SiO_2/CQDs/GCE. Cyclic voltammetry curves in 2.0 mmol/L K_3 [Fe (CN) $_6$] and 0.1 mol/L KCl electrolyte containing 10 mM H_2O_2. **b** Cyclic voltammetry curves with Au@SiO_2/CQDs/GCE in electrolytes containing different concentrations of H_2O_2; scanning rate: 50 mV/s. **c** Cyclic voltammetry curves at different scanning rates of Au@SiO_2 @CQDs/GCE electrode. **d** Graph of the relationship between peak current and square root of scanning rate

of different modified electrodes was estimated by Randles-Sevcik equation.

$$I_P = 2.69 \times 10^5 A D^{1/2} n^{3/2} r^{1/2} C$$

where IP is the peak current value; D is the diffusion coefficient of K_3 [Fe (CN) $_6$], which is (7.6×10^{-6} cm [2] / s); n is the electron transfer number of the reaction system, which is 1; γ is the scanning rate, which is 50 mV/S; and C is the concentration of K_3 [Fe (CN) $_6$], which is 2 mmol/L.

The electroactive surface area of different electrodes was estimated, Au@SiO_2/CQDs/GCE. The electroactive area of the electrode is about 1.42 times of the bare GCE electrode and 2.63 times of the CQDS/GCE electrode (Au@SiO_2/CQDs/GCE). The large surface activity of the electrode can be attributed to the adsorption of CQDS on the surface of Au @ SiO_2. SiO_2 provides a large specific surface area and increases the active area of the electrode. Au provides good conductivity [30] and excellent catalytic activity.

Therefore, electrochemical analysis could be conducted using the electrode modified with Au@SiO_2/CQDs nanocomposites. Figure 10b shows the obtained cyclic voltammetry curve in electrolytes containing different concentrations of H_2O_2 using Au@SiO_2/CQDs/GCE electrode. As shown in the figure, the upward peak is the oxidation process, corresponding to the oxidation peak, and the downward peak is the reduction process, corresponding to the reduction peak. With the increase of H_2O_2 concentration, the oxidation peak potential moved from 0.78 V to 0.76 V, the reduction peak potential moved from 0.53 V to 0.56 V, and the reduction peak current increased significantly with the increase of H_2O_2 concentration, indicating Au@SiO_2/CQDs/GCE electrode has good electrocatalytic activity for the reduction of H_2O_2, which belongs to a typical electrocatalytic reduction process [31].

Cyclic voltammetry curves at different scanning rates of Au@SiO_2 @CQDs/GCE electrodes was studied, as shown in Fig. 10c. With the scan rate increasing from 10 mV/s to 100 mV/s, the peak potential changes little with the scanning rate, and the response of peak current changes obviously. The redox peak current becomes more negative with the correction of oxidation peak current change. The peak current has a good linear relationship with the square root of scanning rate, as shown in Fig. 10d. The black square curve represents the change of oxidation peak current with the square root of scanning rate. The linear equation is I (μ a) = 1.648 (V) 1 / 2 (MV / s) 1 / 2 + 3.096 The linear equation is I (μ a) = - 2.120 (V) 1 / 2 (MV / s) 1 / 2-3.756 (R2 = 0.986). Therefore, the redox reaction on the surface of Au@SiO_2/CQDs/GCE electrode is corresponding to a semi-infinite linear diffusion process [32, 33].

As Au@SiO_2/CQD nanocomposites show better catalytic activity compared to pure CQDs, therefore, Au@SiO_2/CQD-modified glassy carbon electrode was selected to study the ampere response of H_2O_2 to achieve better detection results. Select Au@SiO_2/CQDs/GCE as the working electrode in 2.0 mmol/L $K_3[Fe(CN)_6]$ and 0.1 mol/L KCl electrolyte under the condition of constant voltage. Observe the current change with the addition of different concentrations of H_2O_2; Fig. 11a shows the time–current curve. Obvious current response can be obtained when adding a small dose of 0.2 mM. After each addition of H_2O_2, the maximum response can be reached within 4 s, indicating that the working electrode has a rapid response to H_2O_2. As shown in Fig. 11b, the linear curve of current with the concentration of H_2O_2 is made. The current has a good linear relationship with the concentration of H_2O_2, and the corresponding linear equation is as follows: I (μA) = −0.55 C (mM) − 0.306 (R = 0.98712), and the linear response range is from 0.2 to 18 mM.

The interference of external factors needs to be considered In the process of detecting H_2O_2. Added possible interfering substances (with a concentration of 1mM) such as ascorbic acid, lactic acid, and glucose to the electrolyte solution for testing, the results show that the above substances had no significant impact on the determination of the modified electrode, indicating that the modified electrode had good selectivity under these experimental conditions.

The reproducibility and repeatability of the sensors used for detection are crucial. Before the electrode was used to

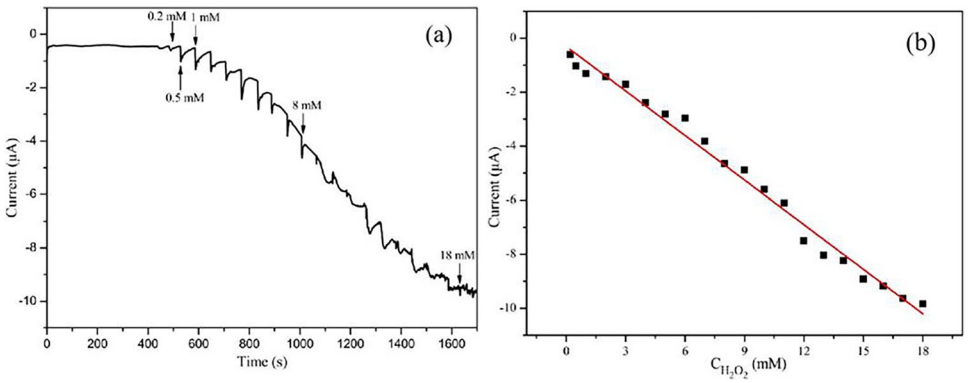

Fig. 11 **a** Amperometric responses of the Au@SiO_2/CQDs/GCE electrode to the successive addition of different concentrations of H_2O_2, **b** linear calibration curve of amperometric responses to the concentration of H_2O_2

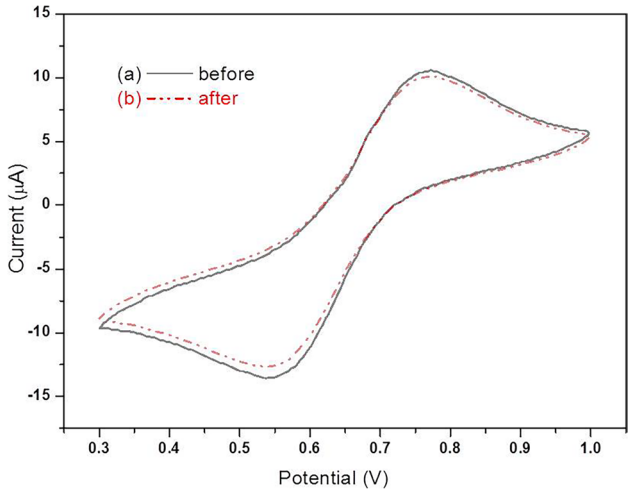

Fig. 12 Cyclic voltammetry curves obtained from GCE modified with Au@SiO_2@CQDs before (**a**) and after (**b**) storage at room temperature for 1 week in a solution containing 5mM H_2O_2

explore stability, it was used in the experiment shown in Fig. 10 and the electrode exhibits good cycling stability after 100 cycles of cyclic scanning. And then keep it in air at room temperature for a week. Figure 12 shows the comparison of GCE modified with Au@SiO_2/CQDs before and after being stored in air without any protection for a week. It can be seen that the oxidation reaction shows a little shift, with a slight decrease in peak current. The results show the stability of the Au@SiO_2/CQD-modified electrode is excellent.

Conclusion

In this study, CQDs were synthesized using a one-step hydrothermal method; moreover, Au@SiO_2/CQD nanocomposites were synthesized using a layer-by-layer wrapping method. The nanocomposites showed excellent electrochemical properties. By constructing a hydrogen peroxide sensor for the sensitive detection of H_2O_2, the minimum detection concentration can reach 0.2 mM, which has the advantages of high sensitivity and fast response. The electrode GCE modified with Au@SiO_2/CQDs exhibits good selectivity and stability in the detection of hydrogen peroxide. Therefore, for H_2O_2 sensors, Au@SiO_2/CQDs nanocomposite materials can become ideal materials.

Author contributions Li H and Wu L proposed the research and guided the project. Deng C and Huang F designed and performed the experiments. Lei H and Ren Li analyzed and discussed the experimental results, Zhang H prepared Figs. 8, 9, and 10; Zhao W and Zhao Q were responsible for stability and selectivity experiments. Li H and Deng C drafted the manuscript. All the authors reviewed and approved the manuscript.

Funding This work was financially supported by the National Natural Science Foundation of China (51702006, 22002002), Shaanxi provincial science and technology planning project (2018JQ2056), the Youth Science and Technology New Star Plan of Shaanxi Province] grant number (2021KJXX-50), the Phytochemistry Key Laboratory of Shaanxi Province (NO.18JS007), and the Natural Science Foundation of Shaanxi Province (2023JCYB120).

Data availability The data that support the findings of this study are openly available.

Declarations

Ethics approval and consent to participate Not applicable.

Competing interests The authors declare no competing interests.

References

1. Aparicio-Martínez E, Ibarra A, Estrada-Moreno IA et al (2019) Flexible electrochemical sensor based on laser scribed graphene/Ag nanoparticles for non-enzymatic hydrogen peroxide detection. Sens Actuators B Chem 301:127101
2. Thanh TD, Balamurugan J, Lee SH et al (2016) Novel porous gold-palladium nanoalloy network-supported graphene as an advanced catalyst for non-enzymatic hydrogen peroxide sensing. Biosens Bioelectron 85:669–678
3. Li H, Yang J, Deng Q et al (2018) Au nanoparticle@ silica@ europium coordination polymer nanocomposites for enhanced fluorescence and more sensitive monitoring reactive oxygen species. Sci China Mater 61(3):401–408
4. Zhang MR, Chen XQ, Pan GB (2017) Electrosynthesis of gold nanoparticles/porous GaN electrode for non-enzymatic hydrogen peroxide detection. Sens Actuators B: Chem 240:142–147
5. Tran HV, Huynh CD, Tran HV et al (2016) Cyclic voltammetry, square wave voltammetry, electrochemical impedance spectroscopy and colorimetric method for hydrogen peroxide detection based on chitosan/silver nanocomposite. Arab J Chem:1–7
6. Tran HV, Trinh AX, Huynh CDF et al (2016) Hydrothermal synthesis of silver/chitosan nanocomposite and application in the electrochemical detection of hydrogen peroxide. Sens Lett 14(1):32–38
7. Yuan T, Meng T, He P et al (2019) Carbon quantum dots: an emerging material for optoelectronic applications. J Mater Chem C 7(23):6820–6835
8. Chan KK, Yap SHK, Yong KT (2018) Biogreen synthesis of carbon dots for biotechnology and nanomedicine applications. Nano-Micro Lett 10(4):1–46
9. Amjadi M, Hallaj T, Asadollahi H et al (2017) Facile synthesis of carbon quantum dot/silver nanocomposite and its application for colorimetric detection of methimazole. Sens Actuators B: Chem 244:425–432
10. Liu H, Yang J, Li Z et al (2019) Hydrogen-bond-induced emission of carbon dots for wash-free nucleus imaging. Anal Chem 91(14):9259–9265
11. Tran HV, Le TA, Giang BL et al (2019) Silver nanoparticles on graphene quantum dots as nanozyme for efficient H2O2 reduction in a glucose biosensor. Mater Res Express 6:115403
12. Jiang X, Li BQ, Qu X et al (2019) Multilayered dual functional SiO_2@ Au@ SiO_2@ QD nanoparticles for simultaneous intracellular heating and temperature measurement. Langmuir 35(19):6367–6378

13. Wang H, Ming S, Zhang L et al (2018) A simple strategy to achieve shape control of Au-$Cu_{2-x}S$ colloidal heterostructured nanocrystals and their preliminary use in organic photovoltaics. Nanoscale 10(25):11745–11749
14. Yang TQ, Peng B, Shan BQ et al (2020) Origin of the photoluminescence of metal nanoclusters: from metal-centered emission to ligand-centered emission. Nanomaterials 10(2):261
15. Zhang H, Li Y, Long X et al (2020) Self-assembled metamaterial perfect absorbers at visible wavelengths using core–shell Au@ SiO_2 meta-atoms. J Mater Chem C 8(37):12876–12885
16. Chen D, Shi J, Shen H (2020) High-dispersed catalysts of core–shell structured Au@ SiO_2 for formaldehyde catalytic oxidation. Chem Eng J 385:123887
17. Montaño-Priede JL, Coelho JP, Guerrero-Martínez A et al (2017) Fabrication of monodispersed Au@ SiO_2 nanoparticles with highly stable silica layers by ultrasound-assisted stober method. J Phys Chem C 121(17):9543–9551
18. Sakthisabarimoorthi A, Dhas SAMB, Jose M (2020) Study on optical nonlinearity of Au@ SiO_2 composite nanoparticles towards photonic applications. Mater Chem Phys 240:122154
19. Li X, Xu Y, Chen Y et al (2019) Dual enhanced electrochemiluminescence of aminated Au@ SiO_2/CdS quantum dot superstructures: electromagnetic field enhancement and chemical enhancement. ACS Appl Mater Interfaces 11(4):4488–4499
20. Li SH, Weng B, Lu KQ et al (2018) Improving the efficiency of carbon quantum dots as a visible light photosensitizer by polyamine interfacial modification. Acta Phys Chim Sin 34:708–718
21. Huang J, Li L, Chen J et al (2020) Broad spectrum response flower spherical-like composites CQDs@ $CdIn_2S_4$/CdS modified by CQDs with up-conversion property for photocatalytic degradation and water splitting. Int J Hydrogen Energy 45(3):1822–1836
22. Wijaya H, Darwan D, Lim KRG et al (2019) Large-Stokes-Shifted Infrared-Emitting InAs–In (Zn) P–ZnSe–ZnS Giant-Shell Quantum Dots by One-Pot Continuous-Injection Synthesis. Chem Mater 31(6):2019–2026
23. Riaz R, Ali M, Maiyalagan T et al (2019) Dye-sensitized solar cell (DSSC) coated with energy down shift layer of nitrogen-doped carbon quantum dots (N-CQDs) for enhanced current density and stability. Appl Surf Sci 483:425–431
24. Wang W, Ji Y, Zhang Y et al (2016) Green preparation of Au nanoparticles for electrochemical detection of H_2O_2. J Semiconduct 37(1):013003
25. Wen S, Miao X, Fan GC et al (2019) Aptamer-Conjugated Au Nanocage/SiO_2 Core–shell bifunctional nanoprobes with high stability and biocompatibility for cellular SERS imaging and near-infrared photothermal therapy. ACS Sens 4(2):301–308
26. Cao N, Zhao F, Zeng B (2020) A novel self-enhanced electrochemiluminescence sensor based on PEI-CdS/Au@ SiO_2@ RuDS and molecularly imprinted polymer for the highly sensitive detection of creatinine. Sens Actuators B: Chem 306:127591
27. Liu M , Deng J , Chen Q et al (2013) Sensitive detection of rutin with novel ferrocene benzyne derivative modified electrodes. Biosens Bioelectron 41:275 – 281
28. Wang X, Wang Y, Shan Y et al (2018) A novel and sensitive electrogenerated chemiluminescence biosensor for detection of p16INK4a gene based on the functional paste-like nanofibers composites-modified screen-printed carbon electrode. J Electroanal Chem 823:368–377
29. Dong W, Ren Y, Zhang Y et al (2017) Synthesis of Pb nanowires-Au nanoparticles nanostructure decorated with reduced graphene oxide for electrochemical sensing. Talanta 165:604–611
30. Lu YY, Li NL, Jia LP et al (2016) The synthesis of Ag@ CQDs composite and its electrochemiluminescence application for the highly selective and sensitive detection of chloride. J Electroanal Chem 781:114–119
31. Wang M, Yin H, Zhou Y et al (2019) A novel photoelectrochemical biosensor for the sensitive detection of dual microRNAs using molybdenum carbide nanotubes as nanocarriers and energy transfer between CQDs and AuNPs. Chem Eng J 365:351–357
32. Zhu P, Zhao Y (2019) Cyclic voltammetry measurements of electroactive surface area of porous nickel: peak current and peak charge methods and diffusion layer effect. Mater Chem Phys 233:60–67
33. Yang MH, Kim DS, Yoon JH et al (2016) Nanopillar films with polyoxometalate-doped polyaniline for electrochemical detection of hydrogen peroxide. Analyst 141(4):1319–1324